nature communications



Article

https://doi.org/10.1038/s41467-024-54485-7

Role of anthropogenic forcing in Antarctic sea ice variability simulated in climate models

Received: 26 February 2024

Accepted: 8 November 2024

Published online: 20 December 2024



Yushi Morioka ¹ M, Liping Zhang ^{2,3}, William Cooke ², Masami Nonaka ¹, Swadhin K. Behera ¹ & Syukuro Manabe⁴

Antarctic sea ice extent has seen a slight increase over recent decades, yet since 2016, it has undergone a sharp decline, reaching record lows. While the precise impact of anthropogenic forcing remains uncertain, natural fluctuations have been shown to be important for this variability. Our study employs a series of coupled model experiments, revealing that with constant anthropogenic forcing, the primary driver of interannual sea ice variability lies in deep convection within the Southern Ocean, although it is model dependent. However, as anthropogenic forcing increases, the influence of deep convection weakens, and the Southern Annular Mode, an atmospheric intrinsic variability, plays a more significant role in the sea ice fluctuations owing to the shift from a zonal wavenumber-three pattern observed in the historical period. These model results indicate that surface air-sea interaction will play a more prominent role in Antarctic sea ice variability in the future.

Antarctic sea ice extent (SIE) has slightly increased in the past few decades¹. Since 2016, however, it has abruptly declined² and remained a record low in 2023³. Natural variability in the atmosphere and ocean such as deepening of the Amundsen Sea Low⁴ and weakening of the Southern Ocean deep convection⁵ is suggested to cause the increasing sea ice trend. The atmospheric zonal wavenumber-three (ZW3)6 pattern induced by extremely warm El Niño/Southern Oscillation (ENSO) in 2015 and the subsequent occurrence of a negative phase of the Southern Annular Mode (SAM)⁷ contributed to the abrupt sea ice decline in 20168. The warming of subsurface Southern Ocean (100-500 m) has also contributed to a weaker stratification thereby sustaining an anomalously low sea ice state afterwards9. Interannual sea ice variability has increased in a recent decade, not solely related to the atmospheric variability¹⁰ but the ocean mixed-layer variability¹¹. However, it is uncertain how the interannual sea ice variability changes in the future under the anthropogenic forcing.

Several studies have discussed the impact of anthropogenic forcing on the future Antarctic sea ice mean state using coupled general circulation models^{12–15}. Most of them have consistently argued the sea

ice decline as the anthropogenic forcing increases. For example, one recent study¹⁶ has discussed that the rate of the sea ice decline is slower in an eddy-permitting coupled model than a lower-resolution coupled model because the northward Ekman heat transport increases in response to stronger westerlies and moderates the Southern Ocean warming. However, the results are inconsistent with other studies using eddy-resolving or -permitting models that simulate increase in poleward heat transport by ocean mesoscale eddies and offset the increase in the northward mean heat transport^{17–20}. Due to complex nature of Southern Ocean circulation, there is a wide disparity among climate models in future projections of sea ice decline associated with the ocean heat transport change²¹.

Little attention has been paid to how the interannual sea ice variability changes in the future under the anthropogenic forcing. A few studies have suggested the impact of future changes in ENSO and the SAM on the sea ice mean state. For example, a majority of coupled models in the sixth phase of the Coupled Model Intercomparison Project (CMIP6) demonstrate that the variance and frequency of ENSO are likely to increase as the anthropogenic forcing increases²².

¹Application Laboratory, VAiG, JAMSTEC, Yokohama, Japan. ²Geophysical Fluid Dynamics Laboratory, Princeton, NJ, USA. ³University Corporation for Atmospheric Research, Boulder, CO, USA. ⁴Atmospheric and Oceanic Sciences Program, Princeton University, Princeton, NJ, USA. © e-mail: morioka@jamstec.go.jp The models projecting stronger ENSO tend to project slower Southern Ocean warming²³ and sea ice reduction²⁴, because of weaker upwelling of subsurface warm Circumpolar Deep Water (CDW) due to weaker intensification of westerlies. However, most of CMIP6 models project poleward shift and intensification of westerlies, representing a positive trend of the SAM²⁵. The positive SAM tends to enhance the equatorward Ekman transport and reduce the coastal sea level around the Antarctic coastline. This could also cause a multidecadal poleward shift of the Antarctic Circumpolar Current²⁶ and a weakening of the Antarctic Slope Current, allowing more warm CDW to flow over the continental slope and enhance sea ice melt^{27,28}.

Besides ENSO and the SAM, the increased precipitation and Antarctic meltwater could also cause a contraction of the Antarctic Bottom Water²⁹, a weakening of the deep convection in the Southern Ocean^{30,31}, and more intrusion of warm CDW over the continental shelf^{32,33}. With the constant anthropogenic forcing, the Southern Ocean deep convection could drive a centennial-scale Antarctic temperature variations^{34,35}. However, the relative importance of future changes in the deep convection, ENSO, and the SAM on the interannual sea ice variability remains unclear. To address these unresolved scientific issues, this study employs a series of coupled model experiments with natural and anthropogenic forcings to identify physical processes underlying the future Antarctic sea ice mean state and variability.

Results

Impact of anthropogenic forcing on Antarctic sea ice mean state The SPEAR MED historical run (see Methods) reasonably captures the observed seasonal cycle of pan-Antarctic SIE climatology (Supplementary Fig. 1a), although it has a low sea ice bias in austral summer, consistent with other CMIP6 models¹². This is mostly due to smaller SIE climatology simulated in the West Pacific sector, Ross Sea, and Amundsen-Bellingshausen Sea (Supplementary Fig. 1d, e, f). With these model biases in mind, clarifying the mean state change under the increasing anthropogenic forcing is helpful for understanding the change in the sea ice variability. Antarctic SIE deviation in the natural forcing run (Fig. 1a) exhibits a low-frequency variability with high values in the 1960s and 2060s and low values in the 2000s. We also find similar fluctuations in Antarctic sea ice area (SIA) and sea ice volume (SIV) deviations (Supplementary Fig. 2a, b), whereas the occurrence number of Polynya events (see Methods) shows a smaller low-frequency variability compared to the observation owing to the lower model resolution (Supplementary Fig. 2c).

The low-frequency variability may originate from a multidecadalcentennial variability of Antarctic SIE in the preindustrial control simulation used for generating ensemble members (Supplementary Fig. 3: see Methods). However, in the natural forcing run, this signature is present in the multi-model mean, implying that it is not purely internal variability. In particular, Antarctic SIE deviation in the natural forcing run captures an increasing trend of the observed one after 2000 (Fig. 1a). This suggests that the observed trend may arise from the natural forcing which includes solar radiation and volcanic aerosols (see Methods). Major volcanic eruptions (Mt. Agung in 1963; El Chichon in 1982; Mt. Pinatubo in 1991) and the associated sharp radiative coolings in the 1960s³⁶, the 1980s³⁷, and the 1990s³⁸ (Supplementary Fig. 2d) appear to slightly affect the sea ice increase on interannual timescale (Fig. 1a; Supplementary Fig. 2a, b). However, its influence on the increasing trend is rather limited. Rather, the decreasing trend in the net radiation at the top of the atmosphere after the late 1990s (Supplementary Fig. 2d) appears to be responsible for the increasing sea ice trend after 2000.

SPEAR_MED shows that when the anthropogenic forcing increased, Antarctic SIE started to decrease after the 2000s (Fig. 1a). The magnitude of negative anomalies after 2016 is similar to the observed one, although the negative anomalies developed gradually rather than in the abrupt manner observed (Fig. 1a). This may underscore a possible impact of increased anthropogenic forcing on the recent decline in sea ice. Antarctic SIE shows a steady decline under the anthropogenic forcing in the future. However, if climate change mitigations are adopted in either 2030 or 2040 (see Methods), Antarctic SIE will gradually recover in this model. The future projection of Antarctic SIE inversely follows that of carbon dioxide (CO₂; Fig. 1b).

In SPEAR_MED natural forcing run with the constant anthropogenic forcing, the net surface heat flux (Fig. 2a) undergoes a low-frequency variability in such a way that more heat releases from the ocean as the sea ice melts and vice versa. When the anthropogenic forcing increases, the net surface heat flux increases positively to warm the ocean (Fig. 2a). This is mostly due to the increase in the sensible heat flux (Supplementary Fig. 4a) and secondarily due to the delayed increase in the shortwave radiation (Supplementary Fig. 4b). We find that latent heat flux and longwave radiation increase negatively to cool the ocean, playing counteracting roles (Supplementary Fig. 4c, d). Furthermore, as the anthropogenic forcing increases, the air temperature in the atmospheric boundary layer increases to warm the ocean and sea ice. The resultant sea ice melting triggers the ice-albedo feedback by yielding an increase in the lower-albedo and ice-free ocean surface³⁹.

In addition to the net surface heat flux, SPEAR_MED demonstrates that surface winds and subsurface ocean heat can also play some roles. Compared to the historical forcing run, the highest emission scenario

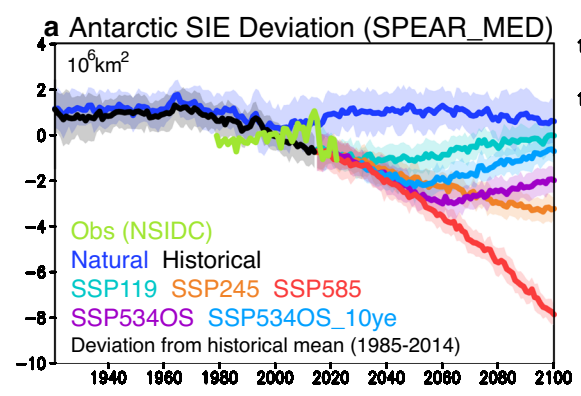
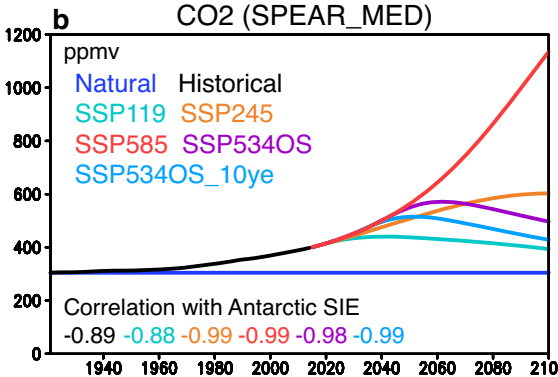


Fig. 1 | **Antarctic sea ice extent (SIE) and carbon dioxide (CO₂) in SPEAR_MED runs. a** Deviation of Antarctic SIE (in 10⁶ km²) from the mean value of the historical period (1985–2014). Here we used the observed mean value of the historical period to calculate the observed SIE deviation (green), while we used the mean value of the



historical run to calculate the simulated SIE deviation. **b** CO_2 (in ppmv) during 1921–2100 used in SPEAR_MED natural, historical, and SSP forcing runs. Correlations with Antarctic SIE deviation for historical and SSP forcing runs are shown in the panel.

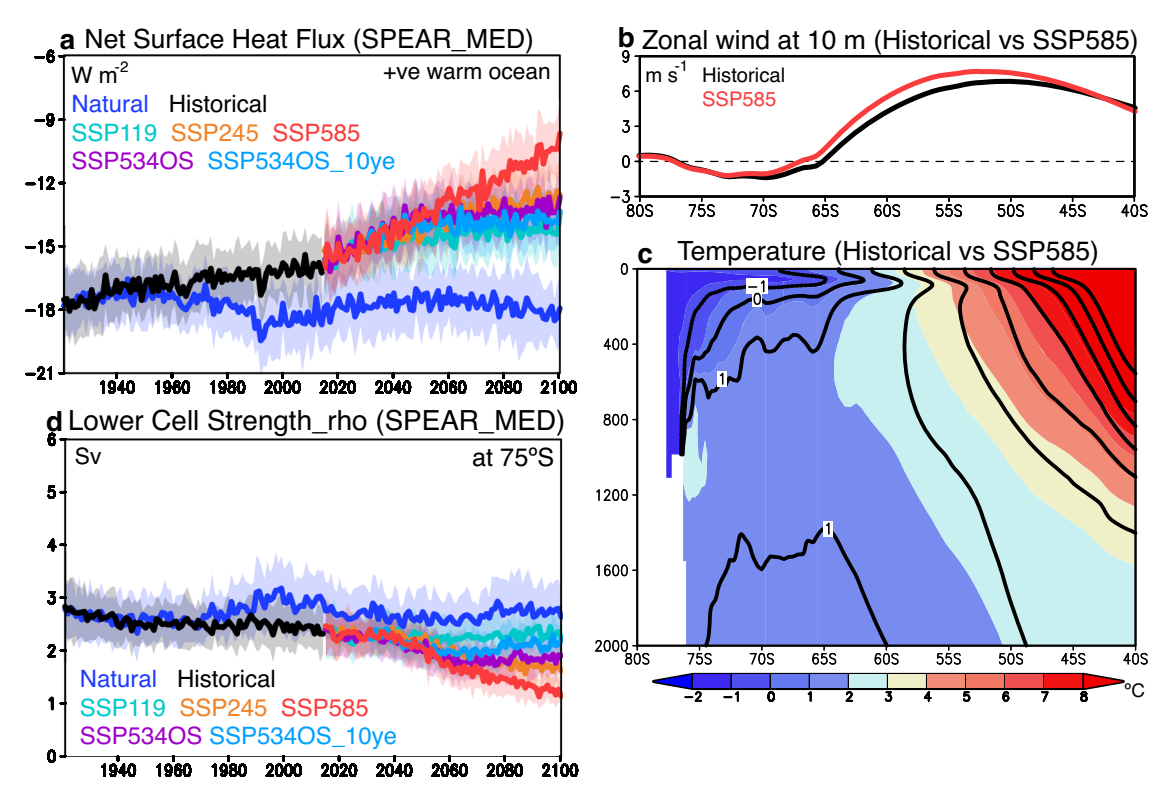


Fig. 2 | Net surface heat flux, zonal-mean zonal wind, ocean potential temperature, and lower cell strength in SPEAR_MED runs. a Net surface heat flux (in W m $^{-2}$) in the Antarctic Sea (region south of 60°S) for 1921–2100 period of SPEAR_MED natural, historical, and SSP forcing runs. Positive values indicate downward heat flux to warm the ocean. b Zonal-mean zonal wind speed at 10 m (in m s $^{-1}$) as a function of latitude for the 30-yr average of the historical (black;

1985–2014) and SSP585 (red; 2071–2100) forcing runs. **c** Latitude-depth cross section of zonal mean ocean potential temperature (in °C) for the 30-yr average of the historical (black contour; 1985-2014) and SSP585 (color; 2071–2100) forcing runs. **d** Same as in (**a**), but for the lower cell strength (LCS; in Sv) on a density space. The LCS index (see Methods) is defined as absolute value of negatively maximum streamfunction on a density space at 75°S near the Antarctic coast.

(i.e., SSP585; see Methods) run projects surface westerlies stronger at higher latitudes (Fig. 2b). The strengthening and poleward shift of westerlies leads to those of upwelling of subsurface warm and saline CDW (Fig. 2c), facilitating the sea ice melt from below. The sea ice melt also influences the deep convection near the Antarctic coast. With the constant anthropogenic forcing, the lower cell strength (LCS; see Methods), which corresponds to the strength of the lower ocean circulation cell used as a potential indicator of the deep convection (Fig. 2d, Supplementary Fig. 5a), undergoes a low-frequency variability, as simulated in the Antarctic SIE deviation (Fig. 1a). Stronger deep convection tends to bring warm CDW to the surface thereby melting sea ice from below and vice versa. When the anthropogenic forcing increases, however, deep convection weakens (Fig. 2d). Even if climate change mitigations are adopted in either 2030 or 2040 (see Methods), the deep convection remains weaker. The weaker deep convection arises from the surface freshening (Supplementary Fig. 5b) associated with the increased precipitation (Supplementary Fig. 5c). The total volume change in the freshwater input by the precipitation is much larger than the increased runoff associated with the Antarctic ice shelf melt (Supplementary Fig. 5d).

In the highest emission scenario run of SPEAR_MED (Fig. 3a), the sea ice steadily declines in the entire Antarctic Sea (region south of 60°S). This translates into surface temperature increase (Supplementary Fig. 6a), positive sea level pressure (SLP) changes in the midlatitudes and negative SLP changes over Antarctica (Supplementary Fig. 6b), representing stronger westerlies associated with a positive trend of the SAM. In the post-2040 mitigation run (Fig. 3b), the sea ice does not significantly change due to the delayed Antarctic SIE minimum in around 2060 (Fig. 1a), whereas in the post-2030 mitigation run

(Fig. 3c), the sea ice shows a significant recovery in the Pacific and Atlantic sectors. Despite these sea ice changes, the surface temperature shows a slightly positive trend along the Antarctic Circumpolar Current (Supplementary Fig. 6c, e), whereas the SLP shows weaker westerlies associated with a negative trend of the SAM (Supplementary Fig. 6d, f).

In the highest emission scenario run of SPEAR_MED, the ocean temperature in the Antarctic Sea (region south of 60°S; Fig. 3d) becomes significantly warmer from the surface down to 2000 m. This is associated with a freshening in the upper 500 m and a salinity increase below (Supplementary Fig. 7a). This leads to a stronger stratification (Supplementary Fig. 7b) and a weaker deep convection. On the other hand, poleward shift and strengthening of westerlies facilitate more poleward advection of warm and saline CDW. Even after employing the climate change mitigations in either 2030 or 2040 (see Methods), the subsurface ocean in the Antarctic Sea continues warming (Fig. 3e, f), despite the cooling of near-surface ocean temperature. The salinity and density changes (Supplementary Fig. 7c-f) resemble those in the highest emission scenario run (Supplementary Fig. 7a, b). Therefore, our models suggest that the weaker deep convection and the associated poleward advection of warm and saline CDW may contribute to the persistence of subsurface ocean warming in the Antarctic Sea.

Role of anthropogenic forcing in Antarctic sea ice interannual variability

In SPEAR_MED natural forcing run with constant anthropogenic forcing, the LCS anomaly shows a significantly negative correlation with Antarctic SIE anomalies on the interannual timescale (Table 1a).

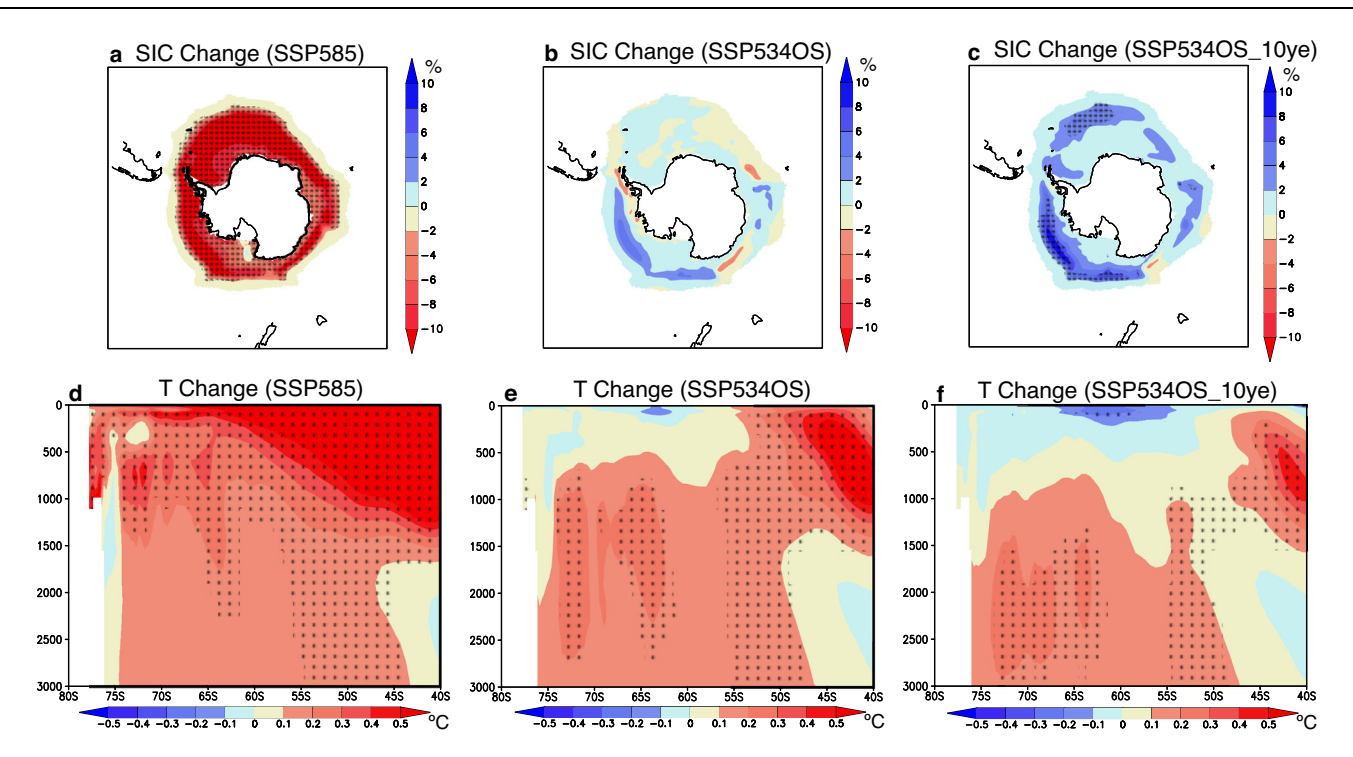


Fig. 3 | Multidecadal changes (2081–2100 minus 2041–2060) in sea ice concentration (SIC) and zonal-mean ocean potential temperature in SPEAR_MED runs. a-c Multidecadal changes in the SIC (in %) from 2041–2060 to 2081–2100 for SPEAR_MED SSP585, SSP534OS, and SSP534OS_10ye forcing runs. Black dots indicate the statistically significant changes that exceed 90% confidence

level using Student's *t*-test. **d-f** Latitude-depth cross-section of multidecadal changes in the zonal-mean ocean potential temperature (color in °C) from 2041–2060 to 2081–2100 for SPEAR_MED SSP585, SSP534OS, and SSP534OS_10ye forcing runs. Black dots indicate the statistically significant changes that exceed 90% confidence level using Student's *t*-test.

The correlation is stronger than that with the SAM and NINO3.4 indices. We also find a similar negative correlation with the mixed-layer depth (MLD, see Methods; Table 1a) averaged in the Antarctic Sea (region south of 60°S). The negative correlations remain significant even for the LCS and MLD anomalies leading the SIE anomalies by one year (Supplementary Table 2a). This indicates that the deepening of the mixed layer in association with the deep convection contributes to the sea ice decrease by entraining subsurface warm water.

When the anthropogenic forcing increases, the SAM shows significantly positive correlations with the SIE anomalies (Table 1a, Supplementary Table 2a), consistent with the historical analysis results⁴⁰. The links with the LCS and NINO3.4 indices get weaker. As the anthropogenic forcing increases, the deep convection weakens, so the LCS index may not measure the deep convection effectively, because it can also be influenced by wind-driven circulation, polynyas, and dense water formation on the continental shelves. Therefore, it is worth examining the correlations with the MLD anomaly that can measure the surface variability rather than deep convection. Indeed, the correlation with the MLD anomaly shows the most change with significantly positive values and gets closer to the correlation with the SAM index (Table 1a, Supplementary Table 2a). This change in sign of the correlation suggests a dynamical change in the sea ice-mixed layer relationship in such a way that the deepening of the mixed layer can contribute to the sea ice increase accompanied by cold dense water. The LCS and MLD measures capture different dynamical behavior in the forced scenarios, resulting in changing correlations with the SIE anomaly, although the detailed dynamical processes for these changed correlations are as yet clear.

The above relationships in SPEAR_MED exhibit seasonal dependency (Table 1b-e). The LCS anomaly (Table 1d) shows significantly negative correlations with Antarctic SIE anomalies during July-September when the strong convection occurs in the Antarctic

Sea. We find a similar negative correlation with the MLD anomaly (Table 1d). The SAM (Table 1e) shows significantly positive correlations during October-December when the westerly wind variability in the stratosphere over the Antarctica is the strongest in a year⁷. We also find that the SAM plays a stronger role in the sea ice variability during April-June and July-September with three months lead (Supplementary Table 2c, d). The link with the SAM and MLD anomaly gets positively stronger as the anthropogenic forcing increases, in particular, during July-September and October-December (Table 1d, e) when the westerly wind shows a larger variability in the stratosphere⁷. The same analysis was conducted for the atmospheric ZW3 index (see Methods), and it is found that the ZW3 (Supplementary Table 1) shows lower correlations with the SIE anomalies than the SAM (Table 1). Furthermore, as the anthropogenic forcing increases, the correlations slightly increase from the natural to historical runs but decrease from the historical to SSP585 forcing run (Supplementary Table 1).

One may wonder whether the expanding role of the SAM under the increasing anthropogenic forcing in SPEAR_MED is a result of intrinsic changes within the SAM itself or a consequence of the diminishing role of the deep convection. The frequency distributions of the SIE and LCS anomalies (Fig. 4a, b) clearly show an increase in weaker anomalies and a decrease in stronger anomalies as the anthropogenic forcing increases, whereas those of the SAM and ENSO indices (Fig. 4c, d) represent no clear changes. We also find that the regression coefficients of the Antarctic SIE anomalies on the LCS anomaly become smaller as the anthropogenic forcing increases (Fig. 5a), whereas those on the SAM index remain similar across the experiments (Fig. 5b). Furthermore, the relationship with ENSO becomes weaker and ultimately negligible as anthropogenic forcing increases (Fig. 5c), which is consistent with the aforementioned correlation analysis (Table 1). These results indicate that the relationship (i.e., regression) between sea ice and the SAM remains the same, but

Table 1 | Yearly and seasonal simultaneous correlations between Antarctic sea ice extent (SIE) and ocean/atmosphere drivers in SPEAR_MED runs

а	Annual mean correlation (30 members)								
	Natural	Historical	SSP534OS	SSP585					
LCS	-0.26*	-0.15*	-0.17*	-0.13*					
MLD	-0.25*	0.21*	0.36*	0.29*					
SAM	0.22*	0.26*	0.39*	0.35*					
NINO3.4	-0.13*	-0.16*	-0.03	0.02					
b	Jan-Mar correlation				С	Apr-Jun c	Apr-Jun correlation		
	Natural	Historical	SSP534OS	SSP585		Natural	Historical	SSP534OS	SSP585
LCS	-0.00	-0.01	0.01	0.01	LCS	-0.26*	-0.25*	-0.16*	-0.22*
MLD	0.21*	0.21*	0.15*	-0.01	MLD	-0.20*	0.50*	0.60*	0.59*
SAM	0.17*	0.18*	0.09*	0.03	SAM	0.29*	0.24*	0.30*	0.25*
NINO3.4	-0.03	-0.09*	0.03	0.02	NINO3.4	0.10*	-0.18*	-0.14*	-0.04
d	Jul-Sep correlation				е	Oct-Dec o	Oct-Dec correlation		
	Natural	Historical	SSP534OS	SSP585		Natural	Historical	SSP534OS	SSP585
LCS	-0.27*	-0.19*	-0.22*	-0.19*	LCS	-0.20*	-0.14*	-0.10*	-0.09*
MLD	-0.17*	0.17*	0.29*	0.24*	MLD	-0.15*	0.27*	0.50*	0.41*
SAM	0.04	0.02	0.14*	0.12*	SAM	0.30*	0.31*	0.43*	0.41*
NINO3.4	-0.12	-0.12*	0.08	0.16*	NINO3.4	-0.07	-0.08*	-0.03	-0.01

a Yearly simultaneous correlation coefficients of annual mean lower cell strength (LCS) anomaly on a density space, mixed-layer depth (MLD) anomaly, Southern Annular Mode (SAM) index, and NINO3.4 index with Antarctic SIE anomalies for 30 ensemble members of SPEAR_MED natural, historical, and SSP forcing runs. We used annual mean anomalies during 1985–2014 period for the natural and historical runs and during 2071–2100 period for the SSP forcing runs. We calculated the correlations across 30 ensemble members over the 30-year period (i.e., 900 points), not for the ensemble mean anomalies, because the ensemble-mean values represent the forced variability. Asterisk indicates statistically significant correlations that exceed 99% confidence level using Student's t-test. b—e Same as in (a), but for January–March, April–June, July–September, and October–December mean anomalies from 30 members of SPEAR_MED natural, historical, and SSP forcing runs, respectively.

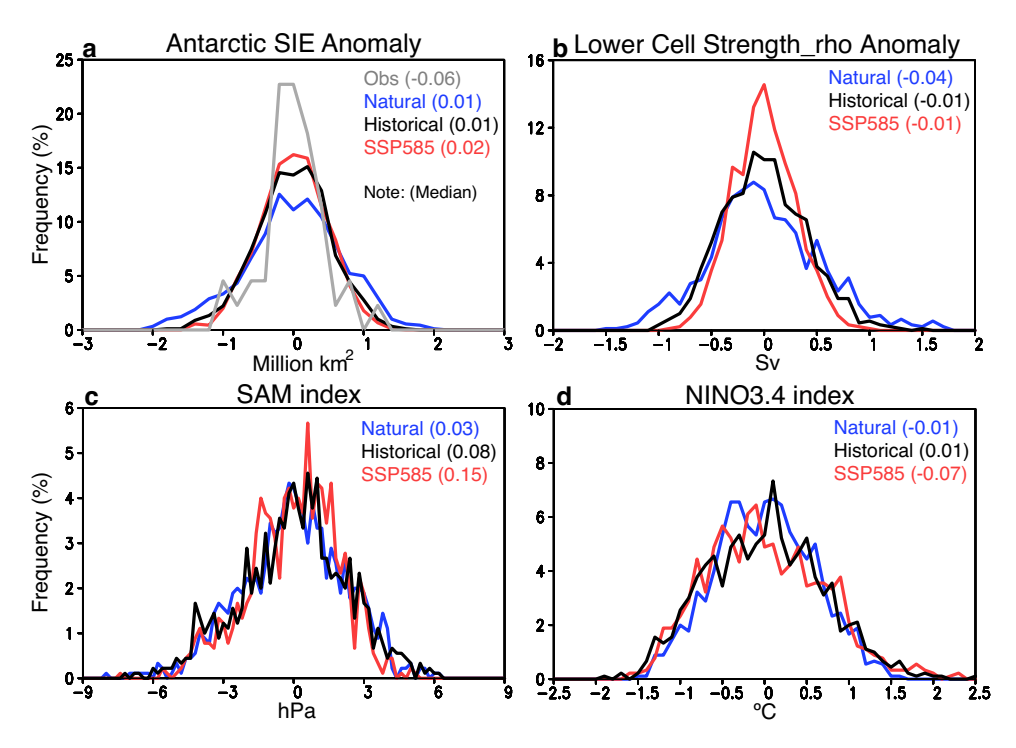


Fig. 4 | Frequency distributions of Antarctic sea ice extent (SIE) anomaly, lower cell strength anomaly, Southern Annual Mode (SAM) and NINO3.4 indices in SPEAR_MED runs. a Frequency distributions (in %) of Antarctic SIE anomalies for the observation and SPEAR_MED natural, historical, and SSP585 forcing runs. Anomalies for the 1979–2022 period of the observation are used, while those for

the 1985–2014 period of the natural and historical forcing runs and for the 2071–2100 period of the SSP585 forcing runs are used. A figure in the parenthesis indicates a median value. **b** Frequency distributions (in %) of the lower cell strength (in Sv) anomalies on a density space for the SPEAR_MED natural, historical, and SSP585 forcing runs. **c**, **d** Same as in (**b**), but for the SAM and NINO3.4 indices.

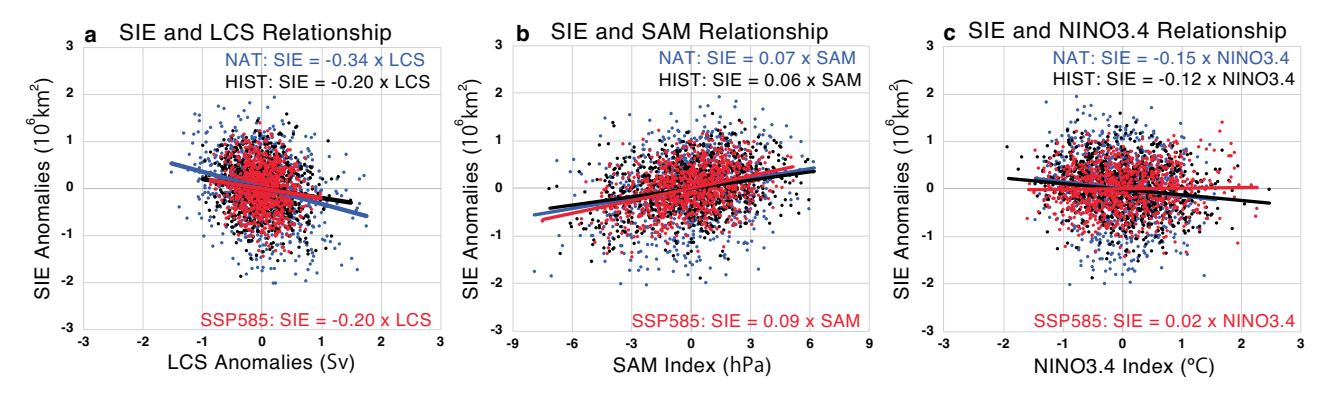


Fig. 5 | Relationships of Antarctic sea ice extent (SIE) anomaly with lower cell strength (LCS) anomaly, Southern Annual Mode (SAM) index, and NINO3.4 index in SPEAR_MED runs. a Scatterplots of Antarctic SIE anomalies (in $10^6\,\mathrm{km^2}$) against the LCS anomalies (in Sv) on a density space for SPEAR_MED natural (blue), historical (black), and SSP585 (red) forcing runs. We used anomalies for 1985–2014

period of the natural and historical forcing runs and for 2071–2100 period of the SSP585 forcing run. Regression line and equation for each of three runs are shown in the panel. **b**, **c** Same as in (**a**), but for the SAM index (in hPa) and NINO3.4 index (in °C).

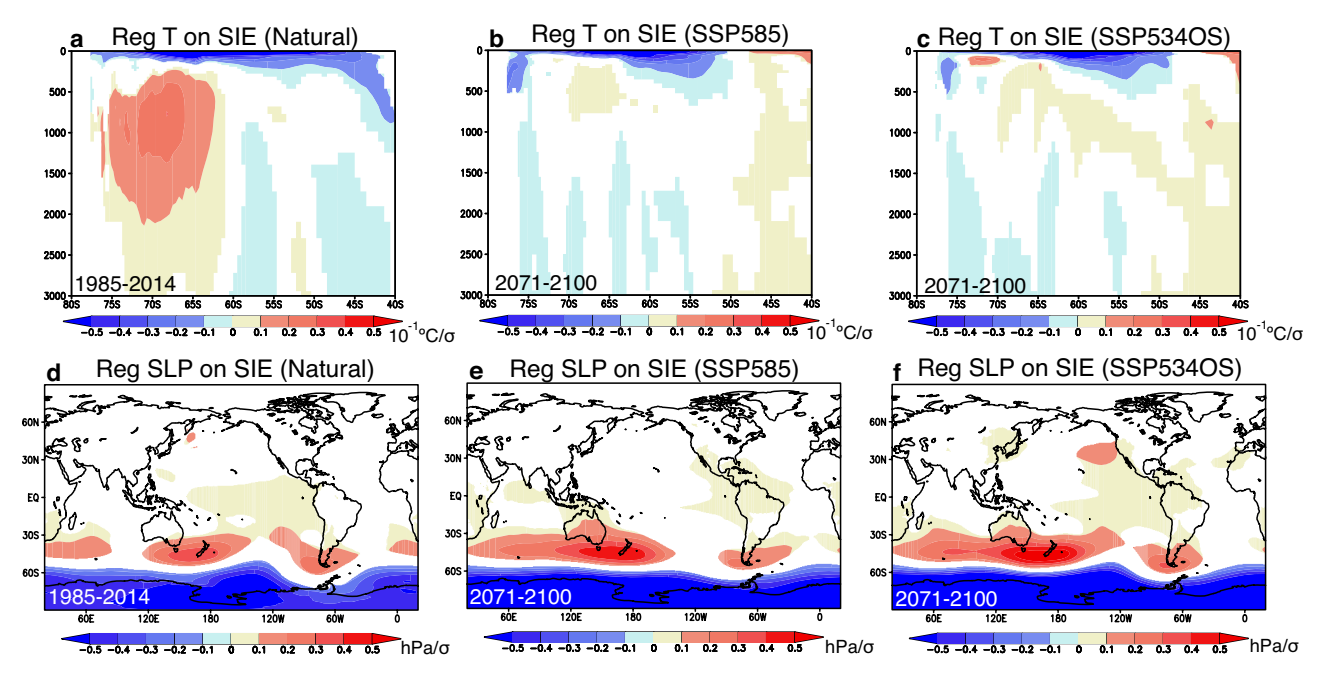


Fig. 6 | Regressions of zonal-mean ocean potential temperature and sea level pressure (SLP) anomalies onto Antarctic sea ice extent (SIE) anomalies in SPEAR_MED runs. a–c Regression coefficients of zonal-mean ocean potential temperature anomalies (in $10^{-1}\,^{\circ}\text{C}/\sigma$) onto standardized Antarctic SIE anomalies for 1985–2014 period of SPEAR_MED natural forcing run and for 2071–2100 period of

SSP585 and SSP534OS forcing runs. We used anomalies from all ensemble members of SPEAR_MED runs to calculate the regression coefficients. Color indicates statistically significant regression coefficients that exceed 99% confidence level using Student's t-test. d-f Same as in (a), but for the regression coefficient of SLP anomalies (in hPa/ σ).

the importance (i.e., correlation) of the SAM increases as a result of the diminishing role of the deep convection.

In SPEAR_MED with constant anthropogenic forcing, sea ice increase is associated with cooler surface temperature and warmer temperature in the subsurface ocean (Fig. 6a). The subsurface heat buildup is accompanied by salinity increase there (Supplementary Fig. 8a). This represents more poleward advection of warm and saline CDW, contributing to lower density there (Supplementary Fig. 9a). When the anthropogenic forcing increases, the links with subsurface heat buildup and salinity increase get weaker, but the links with surface cooler temperature and salinity increase get stronger (Fig. 6b, c; Supplementary Fig. 8b–e; Supplementary Fig. 10c, d). In particular, the salinity increase in the SSP585 forcing run is mostly due to the vertical advection (Supplementary Table 3). This indicates that the deepening

of the mixed-layer associated with the surface cooler temperature and sea ice increase tends to enhance the mixed-layer salinity by entraining subsurface saline water into the mixed layer. The role of surface mixed-layer process gets stronger (Table 1) in association with the weakening role of deep convection.

For the atmospheric variability associated with the sea ice variability under the constant anthropogenic forcing, SPEAR_MED show a signature of the SAM with positive values of the SLP regression in the midlatitudes and negative values over Antarctica but also with a clear signature of the ZW3 during the stronger deep convection period of 1985–2014 (Fig. 6d). We also find a similar ZW3 structure of atmospheric variability for the weaker deep convection periods of 1941–1970 and 2041–2070 (Supplementary Fig. 10a, b, e, f). This suggests that the amplitude of the deep convection may be independent,

not driving the change in the atmospheric relationship in the future. As the anthropogenic forcing increases, the positive and negative SLP patterns become more zonally elongated (Fig. 6e, f; Supplementary Fig. 10g, h), which may explain why the zonally symmetric SAM metric is more strongly related to sea ice in this case. This is also evident in the regressions of surface air temperature anomalies (Supplementary Fig. 11). With the constant anthropogenic forcing, increased SIE is associated with cooler surface temperatures significantly in the Ross Sea and Weddell Sea where the strong deep convection takes place (Supplementary Fig. 11a), whereas as the anthropogenic forcing increases, surface temperature gets warmer in the midlatitudes and cooler in the polar regions, representing the positive SAM-like response (Supplementary Fig. 11b-e). To summarize, the growing influence of the SAM in response to the increasing anthropogenic forcing (Table 1) in SPEAR_MED is linked to the atmospheric variability associated with the sea ice variability becoming a less ZW3-like pattern in contrast to the historical period (Supplementary Table 1).

Dependence on model resolutions and physics

SPEAR_LO with a lower atmospheric resolution shows less reduction in the future SIE than SPEAR_MED (Supplementary Fig. 12a), although there are no clear differences in the LCS on a density space (Supplementary Fig. 12b). The rates of decreases in the SIE deviation and LCS are similar between the two models. This indicates that an increase in atmospheric resolution does not affect the rate of Antarctic SIE decrease in the future, because both models adopt the same atmospheric dynamics. Given these results, the slower rate of future sea ice decrease in other models may be due to increase in their ocean model resolution, but we need to keep in mind a wide disparity among climate models in simulating and predicting the ocean heat uptake and storage in the Southern Ocean²¹.

We obtain similar results for seven CMIP6 models (Supplementary Fig. 12c, d). Here we calculated the LCS index on a depth coordinate because of the limited availability of the model output, so we should note that the results on the deep convection are not directly comparable to the SPEAR model results⁴¹. For example, the SPEAR_MED shows that the amplitude of the LCS index on a density coordinate is smaller than that on a depth space (Supplementary Fig. 12b, d). CMIP6 models show the steady decline of the Antarctic sea ice and deep convection as the anthropogenic forcing increases, although the CMIP6 models have larger spreads than SPEAR_MED. If climate change mitigation is made in 2040 (see Methods), the sea ice effectively recovers but the deep convection remains weaker. This is also evident in the multidecadal changes of the sea ice concentration (SIC) from 2041-2060 to 2081-2100 (Supplementary Fig. 13a, b). In the highest emission scenario run, sea ice continues declining (Supplementary Fig. 13a). This is characterized by surface temperature warming, stronger westerlies (Supplementary Fig. 14a, b), and subsurface ocean warming and salinity increase (Supplementary Fig. 13c, e). On the other hand, in the post-2040 mitigation run, the sea ice effectively recovers (Supplementary Fig. 13b), but Southern Ocean continues warming in association with weaker westerlies, subsurface warming, and salinity increase (Supplementary Fig. 13d, f; Supplementary Fig. 14c, d). All of these mean state changes are consistent with those in SPEAR_MED.

Regarding the relationship with Antarctic sea ice interannual variability, SPEAR_LO demonstrates that a significantly negative correlation with the LCS anomaly does not largely change between constant and increasing anthropogenic forcing, while a significantly positive correlation with the SAM increases as the anthropogenic forcing increases (Supplementary Table 4a). We also find a much weaker link with the NINO3.4 index. On the other hand, four out of seven CMIP6 models (NorESM3-LM, MRI-ESM2-0, IPSL-CM6A-LR, and ACCESS-CM2; Supplementary Table 4c, d, e, f) show increasing roles of the SAM in the sea ice variability under the increasing anthropogenic forcing, whereas only two models (ACCESS-CM2 and CMCC-ESM2;

Supplementary Table 4f, g) show weakening roles of the deep convection in the sea ice variability. Only ACCESS-CM2 shows similar sea ice relationships with the SAM and LCS indices simulated in SPEAR_MED and SPEAR_LO. Therefore, we can conclude that there is not much consistency among the CMIP6 models. The CMIP6 model results are based on a single ensemble member with the same variant level (see Methods) because of the limited availability of ensemble members, so further mechanistic research using more ensemble members is required to better understand the extent of the applicability of these model results in the future.

Discussion

This study has identified the relative roles of deep convection and the SAM in the Antarctic sea ice interannual variability under the anthropogenic forcing. Both SPEAR_MED and SPEAR_LO models have demonstrated that with constant anthropogenic forcing, the Southern Ocean deep convection has the largest role in the sea ice variability, but as the anthropogenic forcing increases, the deep convection weakens, and the SAM plays a more prominent role in the sea ice variability. This involves the shift of the atmospheric variability associated with the sea ice variability to a more symmetric SAM-like pattern, from the ZW3-like pattern observed in the historical period (Fig. 6; Supplementary Table 1). Furthermore, the role of the surface mixed-layer process increases (Table 1) in association with the weakening role of deep convection. These model results indicate a stronger role of surface air-sea interaction in the Antarctic sea ice variability in the future. We have also confirmed the increasing role of the SAM in four out of seven CMIP6 models, while only two models show the decreasing role of the deep convection, representing a large diversity among the CMIP6 models.

Most of the CMIP6 models including the SPEAR models do not have sufficient ocean resolutions to simulate ocean mesoscale eddies with less than 10 km at latitudes higher than 60°S^{42,43}. The mesoscale eddies transport heat poleward across the Antarctic Circumpolar Current and play a counteracting role in northward Ekman heat transport by westerlies. When the anthropogenic forcing increases, the eddy activity is expected to increase with stronger westerlies so that the increase in the poleward heat transport further compensates for the increase in the equatorward mean heat transport^{19,20}. However, a previous study¹⁶ claimed that the sea ice declines at a slower rate in an eddy-permitting coupled model. It is uncertain whether the results are model dependent, so follow-up studies using other eddy-resolving or permitting coupled models are required to verify the role of ocean mesoscale eddies in the future Antarctic sea ice mean state and variability.

Both SPEAR MED/LO and CMIP6 models have demonstrated that ENSO plays a limited role in Antarctic sea ice variability under the increasing anthropogenic forcing. One possible reason for this relationship is that the Antarctic sea ice anomalies associated with ENSO tend to have a dipole structure with opposite signs in the Pacific and Atlantic sectors^{8,44,45}, so that the zonal-mean Antarctic sea ice anomalies associated with ENSO become much smaller. ENSO may influence the SAM through atmospheric teleconnections such as the Pacific-South American mode (PSA)⁴⁶, but ENSO-related atmospheric variability is accompanied by a wavenumber three or four structure in the midlatitudes⁴⁷ and its influence on the SAM depends on the spatial patterns of ENSO 48 . Seasonal observed correlations between ENSO and the SAM are not so high with a range of -0.06 (July-September) to -0.37 (October-December) for the satellite period (1982-2022), so ENSO influence on sea ice variability is much weaker than that of the SAM and deep convection.

Finally, this study has not separated anthropogenic forcing into the individual roles of greenhouse gases, aerosols, and ozone depletion, so the relative influence of them on the sea ice variability remains unclarified. In the past few decades, the ozone depletion tends to cause stronger westerlies associated with a positive trend of the SAM⁴⁹. This leads to sea ice increase through northward Ekman heat transport on an interannual timescale, whereas on a decadal timescale, sea ice declines through upwelling of subsurface warm water⁵⁰. The magnitude and period of the two-timescale response to the ozone depletion vary among climate models⁵¹. In the future, the ozone is expected to recover owing to a decrease in ozone depleting gases, so the influence of ozone-depleting gases on the westerlies and sea ice becomes weaker and overwhelmed by greenhouse gases increase⁵². In our model experiments, we adopted a single emission scenario for ozonedepleting substances (see Methods), so further studies using different emission scenarios would be required to elucidate the impact of ozone-depleting substances on the Antarctic sea ice variability. Furthermore, the cooling effect of volcanic aerosols on the Antarctic sea ice is evident in the natural and historical forcing runs on the interannual timescale (Fig. 1a). However, the influence of future volcanic and anthropogenic aerosols remains uncertain. Further studies are needed to better understand the relative roles of these anthropogenic forcings in the Antarctic sea ice mean state and variability.

Methods

Sea ice data and ocean/atmosphere indicators

As the observational reference, we used daily SIC data with 25 km horizontal resolution during 1979–2022, which is provided from NSIDC and based on Nimbus-7 SMMR and DMSP SSM/I-SSMIS Passive Microwave Data, Version 2⁵³. We defined the SIE and SIA as the total surface area with the SIC greater than 15% and the total surface area multiplied by the SIC for both observations and model simulations, respectively. We also calculated the SIV as the total surface area multiplied by the SIC and sea ice thickness from the model simulations.

To explore a link with subsurface ocean variability in the Antarctic Sea, we calculated a LCS on a density space using the absolute value of the minimum zonal mean meridional overturning streamfunction at 75°S near Antarctic coast where the strong deep convection occurs. We used the LCS as a potential indictor for the strength of the deep convection, but it should be noted that the LCS can also be influenced by wind driven circulation, polynyas and dense water formation on the continental shelves. For comparison with other climate models providing subsurface ocean variables on a depth space, we also calculated the LCS on a depth space using the absolute value of the minimum meridional overturning streamfunction south of 60°S following a previous study⁵.

For the link with large-scale atmosphere and ocean variability, we computed the Southern Annual Mode (SAM) index, which is based on Antarctic Oscillation index (AAO)⁵⁴ and defined as a difference in the zonally averaged SLP between 40°S and 65°S. Among the other climate modes existing in the southern high latitudes⁵⁵, the zonal wavenumber three (ZW3) pattern, a predominant atmospheric winter mode⁵⁶, can also affect the entire Antarctic sea ice^{6,55}. We calculated the ZW3 index⁵⁷ which is originally defined as the average values of standardized SLP anomalies over the three selected regions (latitudes 45-50°S and longitudes 45-60°E, 161-171°E, and 71-81°W), which is different from the recently introduced ZW3 index⁵⁸. We also used the conventional NINO3.4 index, which is defined as the SST anomalies in the centraleastern tropical Pacific (5°S-5°N, 170°W-120°W). For calculation of anomalies, we removed the monthly mean and linear trend using the least squares method over a 30-yr period of our interest. Using the detrended anomalies, we calculated the correlations and regressions.

Coupled general circulation model experiments

To explore Antarctic sea ice variability, we used two coupled general circulation models at National Oceanic and Atmospheric Administration (NOAA)/Geophysical Fluid Dynamics Laboratory (GFDL), called Seamless System for Prediction and Earth System Research Low-Resolution (SPEAR_LO)⁵⁹ and Medium-Resolution (SPEAR_MED)⁵⁹. Both

the SPEAR LO and SPEAR MED are comprised of AM4 atmospheric and LM4 land surface models^{60,61} and the MOM6 ocean and SIS2 sea ice models⁶². These model versions are the same between SPEAR LO and SPEAR MED, but the only difference between them is the atmospheric horizontal resolution with ~100 km and 50 km, respectively, but both models have 33 levels in the vertical with the model top at 1 hPa. The ocean and sea ice components have a nominal horizontal resolution of 1° with a gradual increase to 1/3° in the meridional direction toward the tropics. The ocean model has 75 layers in the vertical that include 30 layers in the top 100 m with a finer resolution. It uses a hybrid vertical coordinate which is based on a function of height in the upper ocean (a z-layer coordinate), transitioning to isopycnal layers in the interior ocean. The ocean model employs a simplified energetics-based parameterization for the planetary boundary layer (ePBL)⁶³ which provides vertical diffusivity and viscosity as well as the depth of active mixing (i.e., the boundary layer thickness). The interior diapycnal mixing is also parameterized as a function of the resolved shear and the flux Richardson number⁶⁴. Due to a coarse resolution, the effects of mesoscale eddies are parameterized by an eddy overturning stream function which estimates the production and dissipation of subgridscale mesoscale kinetic energy balanced by the release of resolved available potential energy 65,66 . We used the model output of the mixedlayer depth defined as the depth at which the ocean potential density increases by 0.03 kg m⁻³ from the surface.

To explore the role of anthropogenic forcing in Antarctic sea ice variability, we analyzed natural radiative forcing, historical radiative forcing, and several future emission scenario runs, called Shared Socio-economic Pathways (SSP) runs, from 1921 to 2100 (Fig. 1b; Supplementary Fig. 2d). For the natural forcing run, we selected 30 initial conditions with 20 years apart from model years 101 to 681 of the pre-industrial control simulation (Supplementary Fig. 3) in which the greenhouse gases, anthropogenic aerosols, land use⁶⁷, solar radiations and volcanic aerosols⁶⁸ set to be constant at 1850 level. Then, we generated 30 ensemble members from 1921 to 2014 which are forced with the constant greenhouse gases, anthropogenic aerosols and land use at 1921 level but with the observed solar radiation and volcanic aerosols. We extended the natural forcing run from 2015 to 2100 using the constant greenhouse gases, anthropogenic aerosols and land use at 1921 level. For the solar radiation, we used a synthetic estimate of solar irradiance changes based on the observed solar cycle, while for the volcanic aerosols, we used the long-term mean values during 1851-2014 with a linear transition from the observed values in 2014 to the estimated values after 2024.

In the historical forcing run, we used the same 30 initial conditions as the natural forcing runs but generated 30 ensemble members from 1921 to 2014 using the observed greenhouse gases, anthropogenic aerosols, land use, solar radiation and volcanic aerosols. In the future scenario runs, we extended the historical forcing run from 2015 to 2100 using different scenario-based anthropogenic forcing⁶⁹, anthropogenic aerosols, land use, solar radiation and volcanic aerosols. Here we conducted the lowest emission SSP1-1.9 scenario (SSP119) run, the medium emission SSP2-4.5 scenario (SSP245) run, and the highest emission SSP5-8.5 scenario (SSP585⁷⁰) run. To explore the impact of climate change mitigation on Antarctic sea ice variability, we used the SSP5-3.4 overshoot scenario (SSP534OS or post-2040 mitigation) run which follows the SSP585 scenario until 2040 but the radiative forcings rapidly decrease to the negative emission level after around 2070⁷¹. To further explore the influence of timing of climate change mitigation, we performed 10-year earlier SSP5-3.4 overshoot scenario (SSP534O-S 10ye or post-2030 mitigation) run. For ozone-depleting substances, we follow a single emission scenario across these future runs as a result of Montreal Protocol72 in which the concentrations and radiative forcing contributions are assumed to strongly reduce with no substantial variations until 2100. We analyzed monthly output of the model experiments and calculated monthly anomalies by removing the

monthly mean and linear trend using the least squares method over a 30-year period of our interest.

Other coupled general circulation model experiments

To explore the dependence of results on model resolutions and physics, we employ a series of natural forcing, historical forcing, and future scenario runs provided from the sixth Coupled Model Intercomparison Project (CMIP6)⁷³. Because of the limited availability for the climate change mitigation (i.e., SSP534OS) run, we selected seven CMIP6 models with the same variant level with realization, initialization, physics and forcing (i.e., rlilp1f1). These consist of CanESM5⁷⁴, NorESM2-LM⁷⁵, MRI-ESM2-O⁷⁶, IPSL-CM6A-LR⁷⁷, ACCESS-CM2⁷⁸, CMCC-ESM2⁷⁹, EC-Earth3-Veg⁸⁰. We downloaded yearly output of the model experiments and calculated yearly anomalies by removing the annual mean and linear trend using the least squares method over a 30-yr period of our interest.

Data availability

The observed daily sea ice concentration is available from NSIDC website: https://doi.org/10.5067/MPYG15WAA4WX. The SPEAR large ensembles of historical and future forcing runs are available from NOAA/GFDL website: https://www.gfdl.noaa.gov/spear_large_ensembles/. The CMIP6 model output is available from USA, PCMDI/LLNL website: https://esgf-node.llnl.gov/projects/cmip6/.

Code availability

All observational and modelling analysis was carried out with the use of open-source code with Fortran and Grads. Due to the large data size, only sample codes used for the numerical analysis are provided here: https://zenodo.org/records/13667134. Other analysis codes are also available from the corresponding author upon request.

References

- Parkinson, C. L. A 40-y record reveals gradual Antarctic sea ice increases followed by decreases at rates far exceeding the rates seen in the Arctic. Proc. Natl Acad. Sci. 116, 14414–14423 (2019).
- Turner, J. et al. Unprecedented springtime retreat of Antarctic sea ice in 2016. Geophys. Res. Lett. 44, 6868–6875 (2017).
- 3. Purich, A. & Doddridge, E. W. Record low Antarctic sea ice coverage indicates a new sea ice state. Commun. Earth Environ. 4, 314 (2023).
- Meehl, G. A., Arblaster, J. M., Bitz, C. M., Chung, C. T., & Teng, H. Antarctic sea-ice expansion between 2000 and 2014 driven by tropical Pacific decadal climate variability. *Nat. Geosci.* 9, 590–595 (2016).
- Zhang, L., Delworth, T. L., Cooke, W. & Yang, X. Natural variability of Southern Ocean convection as a driver of observed climate trends. Nat. Clim. Change 9, 59–65 (2019).
- Raphael, M. N. The influence of atmospheric zonal wave three on Antarctic sea ice variability. J. Geophys. Res. Atmos. 112, D12112 (2007).
- Thompson, D. W. & Wallace, J. M. Annular modes in the extratropical circulation. Part I: month-to-month variability. J. Clim. 13, 1000–1016 (2000).
- Stuecker, M. F., Bitz, C. M. & Armour, K. C. Conditions leading to the unprecedented low Antarctic sea ice extent during the 2016 austral spring season. Geophys. Res. Lett. 44, 9008–9019 (2017).
- Zhang, L. et al. The relative role of the subsurface Southern Ocean in driving negative Antarctic Sea ice extent anomalies in 2016–2021. Commun. Earth Environ. 3, 302 (2022).
- Schroeter, S., O'Kane, T. J. & Sandery, P. A. Antarctic sea ice regime shift associated with decreasing zonal symmetry in the Southern Annular Mode. Cryosphere 17, 701–717 (2023).
- Hobbs, W. et al. Observational evidence for a regime shift in summer Antarctic sea ice. J. Clim. 37, 2263–2275 (2024).

- Roach, L. A. et al. Antarctic sea ice area in CMIP6. Geophys. Res. Lett. 47, e2019GL086729 (2020).
- Bracegirdle, T. J. et al. Twenty first century changes in Antarctic and Southern Ocean surface climate in CMIP6. Atmos. Sci. Lett. 21, e984 (2020).
- Holmes, C. R., Bracegirdle, T. J. & Holland, P. R. Antarctic sea ice projections constrained by historical ice cover and future global temperature change. *Geophys. Res. Lett.* 49, e2021GL097413 (2022).
- Casagrande, F., Stachelski, L. & de Souza, R. B. Assessment of Antarctic sea ice area and concentration in Coupled Model Intercomparison Project Phase 5 and Phase 6 models. *Int. J. Climatol.* 43, 1314–1332 (2023).
- Rackow, T. et al. Delayed Antarctic sea-ice decline in highresolution climate change simulations. *Nat. Commun.* 13, 637 (2022).
- 17. Meredith, M. P. & Hogg, A. M. Circumpolar response of Southern Ocean eddy activity to a change in the Southern Annular Mode. *Geophys. Res. Lett.* **33**, 16 (2006).
- Screen, J. A., Gillett, N. P., Stevens, D. P., Marshall, G. J. & Roscoe, H. K. The role of eddies in the Southern Ocean temperature response to the southern annular mode. J. Clim. 22, 806–818 (2009).
- Farneti, R., Delworth, T. L., Rosati, A. J., Griffies, S. M. & Zeng, F. The role of mesoscale eddies in the rectification of the Southern Ocean response to climate change. *J. Phys. Oceanogr.* 40, 1539–1557 (2010).
- Morrison, A. K. & Hogg, A. M. On the relationship between Southern Ocean overturning and ACC transport. J. Phys. Oceanogr. 43, 140–148 (2013).
- 21. Sallée, J. B. Southern ocean warming. *Oceanography* 31, 52–62 (2018).
- Cai, W. et al. Anthropogenic impacts on twentieth-century ENSO variability changes. *Nat. Rev. Earth Environ.* 4, 407–418 (2023).
- 23. Wang, G. et al. Future Southern Ocean warming linked to projected ENSO variability. *Nat. Clim. Change* **12**, 649–654 (2022).
- Cai, W. et al. Antarctic shelf ocean warming and sea ice melt affected by projected El Niño changes. Nat. Clim. Change 13, 235–239 (2023).
- Goyal, R., Gupta, A. S., Jucker, M. & England, M. H. Historical and projected changes in the Southern Hemisphere surface westerlies. *Geophys. Res. Lett.* 48, e2020GL090849 (2021).
- Yamazaki, K., Aoki, S., Katsumata, K., Hirano, D. & Nakayama, Y. Multidecadal poleward shift of the southern boundary of the Antarctic Circumpolar Current off East Antarctica. Sci. Adv. 7, eabf8755 (2021).
- Spence, P. et al. Rapid subsurface warming and circulation changes of Antarctic coastal waters by poleward shifting winds. *Geophys. Res. Lett.* 41, 4601–4610 (2014).
- Thompson, A. F., Stewart, A. L., Spence, P. & Heywood, K. J. The Antarctic Slope Current in a changing climate. Rev. Geophys. 56, 741–770 (2018).
- 29. Orsi, A. H., Johnson, G. C. & Bullister, J. L. Circulation, mixing, and production of Antarctic Bottom Water. *Prog. Oceanogr.* **43**, 55–109 (1999).
- 30. de Lavergne, C. et al. Cessation of deep convection in the open Southern Ocean under anthropogenic climate change. *Nat. Clim. Change* **4**, 278–282 (2014).
- 31. Gjermundsen, A. et al. Shutdown of Southern Ocean convection controls long-term greenhouse gas-induced warming. *Nat. Geosci.* **14**, 724–731 (2021).
- Schmidtko, S., Heywood, K. J., Thompson, A. F. & Aoki, S. Multidecadal warming of Antarctic waters. Science 346, 1227–1231 (2014).

- Li, Q., England, M. H., Hogg, A. M., Rintoul, S. R. & Morrison, A. K. Abyssal ocean overturning slowdown and warming driven by Antarctic meltwater. *Nature* 615, 841–847 (2023).
- Martin, T., Park, W. & Latif, M. Multi-centennial variability controlled by Southern Ocean convection in the Kiel Climate Model. *Clim. Dyn.* 40, 2005–2022 (2013).
- Pedro, J. B. et al. Southern Ocean deep convection as a driver of Antarctic warming events. *Geophys. Res. Lett.* 43, 2192–2199 (2016).
- Hansen, J. E., Wang, W. C. & Lacis, A. A. Mount Agung eruption provides test of a global climatic perturbation. Science 199, 1065–1068 (1978).
- Hofmann, D. J. Perturbations to the global atmosphere associated with the El Chichon volcanic eruption of 1982. Rev. Geophys. 25, 743–759 (1987).
- Hansen, J., Lacis, A., Ruedy, R. & Sato, M. Potential climate impact of Mount Pinatubo eruption. Geophys. Res. Lett. 19, 215–218 (1992).
- Riihelä, A., Bright, R. M. & Anttila, K. Recent strengthening of snow and ice albedo feedback driven by Antarctic sea-ice loss. *Nat.* Geosci. 14, 832–836 (2021).
- Doddridge, E. W. & Marshall, J. Modulation of the seasonal cycle of Antarctic sea ice extent related to the Southern Annular Mode. Geophys. Res. Lett. 44, 9761–9768 (2017).
- Downes, S. M. & Hogg, A. M. Southern Ocean Circulation and Eddy Compensation in CMIP5 Models. J. Clim. 26, 7198–7220 (2013).
- Chelton, D. B., DeSzoeke, R. A., Schlax, M. G., El Naggar, K. & Siwertz, N. Geographical variability of the first baroclinic Rossby radius of deformation. J. Phys. Oceanogr. 28, 433–460 (1998).
- Hallberg, R. Using a resolution function to regulate parameterizations of oceanic mesoscale eddy effects. *Ocean Model.* 72, 92–103 (2013).
- Yuan, X. & Martinson, D. G. The Antarctic dipole and its predictability. Geophys. Res. Lett. 28, 3609–3612 (2001).
- Yuan, X. ENSO-related impacts on Antarctic sea ice: a synthesis of phenomenon and mechanisms. *Antarct. Sci.* 16, 415–425 (2004).
- Mo, K. C. & Paegle, J. N. The Pacific-South American modes and their downstream effects. Int. J. Climatol. 21, 1211–1229 (2001).
- Ding, Q., Steig, E. J., Battisti, D. S. & Wallace, J. M. Influence of the tropics on the southern annular mode. *J. Clim.* 25, 6330–6348 (2012).
- 48. Yu, J. Y., Paek, H., Saltzman, E. S. & Lee, T. The early 1990s change in ENSO-PSA-SAM relationships and its impact on Southern Hemisphere climate. *J. Clim.* **28**, 9393–9408 (2015).
- Previdi, M. & Polvani, L. M. Climate system response to stratospheric ozone depletion and recovery. Q. J. R. Meteorol. Soc. 140, 2401–2419 (2014).
- Ferreira, D., Marshall, J., Bitz, C. M., Solomon, S. & Plumb, A. Antarctic Ocean and sea ice response to ozone depletion: a two-timescale problem. J. Clim. 28, 1206–1226 (2015).
- Seviour, W. J. M. et al. The Southern Ocean sea surface temperature response to ozone depletion: a multimodel comparison. *J. Clim.* 32, 5107–5121 (2019).
- Arblaster, J. M., Meehl, G. A. & Karoly, D. J. Future climate change in the Southern Hemisphere: Competing effects of ozone and greenhouse gases. *Geophys. Res. Lett.* 38, 2 (2011).
- DiGirolamo, N. E., Parkinson C. L., Cavalieri D. J., Gloersen, P. & Zwally H. J. updated yearly. Sea Ice Concentrations from Nimbus-7 SMMR and DMSP SSM/I-SSMIS Passive Microwave Data, Version 2. Boulder, Colorado USA. NASA National Snow and Ice Data Center Distributed Active Archive Center. https://doi.org/10.5067/ MPYG15WAA4WX.
- Gong, D. & Wang, S. Definition of Antarctic oscillation index. Geophys. Res. Lett. 26, 459–462 (1999).

- Yuan, X. & Li, C. Climate modes in southern high latitudes and their impacts on Antarctic sea ice. J. Geophys. Res. Oceans 113, C06S91 (2008).
- 56. van Loon, H. & Jenne, R. L. The zonal harmonic standing waves in the Southern Hemisphere. *J. Geophys. Res.* **77**, 992–1003 (1972).
- 57. Raphael, M. N. A zonal wave 3 index for the Southern Hemisphere. *Geophys. Res. Lett.* **31**, L23212 (2004).
- 58. Goyal, R., Jucker, M., Gupta, A. S. & England, M. H. A new zonal wave-3 index for the Southern Hemisphere. *J. Clim.* **35**, 5137–5149 (2022).
- Delworth, T. L. et al. SPEAR: The next generation GFDL modeling system for seasonal to multidecadal prediction and projection. J. Adv. Model. Earth Syst. 12, e2019MS001895 (2020).
- Zhao, M. et al. The GFDL global atmosphere and land modelAM4.0/ LM4.0: 1. Simulation characteristics with prescribed SSTs. J. Adv. Model. Earth Syst. 10, 691–734 (2018).
- Zhao, M. et al. The GFDL global atmosphere and land modelAM4.0/ LM4.0: 2. model description, sensitivity studies, and tuning strategies. J. Adv. Model. Earth Syst. 10, 735–769 (2018).
- 62. Adcroft, A. et al. The GFDL global ocean and sea ice modelOM4.0: model description and simulation features. *J. Adv. Model. Earth* Syst. **11**, 3167–3211 (2019).
- 63. Reichl, B. G. & Hallberg, R. A simplified energetics based planetary boundary layer (ePBL) approach for ocean climate simulations. *Ocean Model.* **132**, 112–129 (2018).
- Jackson, L., Hallberg, R. & Legg, S. A parameterization of sheardriven turbulence for Ocean Climate Models. *J. Phys. Oceanogr.* 38, 1033–1053 (2008).
- 65. Jansen, M. F., Held, I. M., Adcroft, A. & Hallberg, R. Energy budget-based backscatter in an eddy permitting primitive equation model. Ocean Model. **94**, 15–26 (2015).
- Marshall, D. P. & Adcroft, A. J. Parameterization of ocean eddies: potential vorticity mixing, energetics and Arnold's first stability theorem. *Ocean Model.* 32, 188–204 (2010).
- Hurtt, G. C. et al. Harmonization of global land use change and management for the period 850–2100 (LUH2) for CMIP6. Geosci. Model Dev. 13, 5425–5464 (2020).
- Meinshausen, M. et al. Historical greenhouse gas concentrations for climate modelling (CMIP6). Geosci. Model Dev. 10, 2057–2116 (2017).
- Meinshausen, M. et al. The shared socio-economic pathway (SSP) greenhouse gas concentrations and their extensions to 2500. Geosci. Model Dev. 13, 3571–3605 (2020).
- O'Neill, B. C. et al. The Scenario Model Intercomparison Project (ScenarioMIP) for CMIP6. Geosci. Model Dev. 9, 3461–3482 (2016).
- Delworth, T. L., Cooke, W. F., Naik, V., Paynter, D. & Zhang, L. A weakened AMOC may prolong greenhouse gas-induced Mediterranean drying even with significant and rapid climate change mitigation. *Proc. Natl Acad. Sci.* 119, e2116655119 (2022).
- 72. Velders, G. J. M. & Daniel, J. S. Uncertainty analysis of projections of ozone-depleting substances: mixing ratios, EESC, ODPs, and GWPs. *Atmos. Chem. Phys.* **14**, 2757–2776 (2014).
- Eyring, V. et al. Overview of the Coupled Model Intercomparison Project Phase 6 (CMIP6) experimental design and organization. Geosci. Model Dev. 9, 1937–1958 (2016).
- 74. Swart, N. C. et al. The Canadian Earth System Model version 5 (CanESM5.0.3). *Geosci. Model Dev.* **12**, 4823–4873 (2019).
- Seland, Ø. et al. Overview of the Norwegian Earth System Model (NorESM2) and key climate response of CMIP6 DECK, historical, and scenario simulations. Geosci. Model Dev. 13, 6165–6200 (2020).
- Yukimoto, S. et al. The Meteorological Research Institute Earth System Model version 2.0, MRI-ESM2. 0: description and basic evaluation of the physical component. J. Meteorol. Soc. Jpn. Ser. II 97, 931–965 (2019).

- Boucher, O. et al. Presentation and evaluation of the IPSL-CM6A-LR climate model. J. Adv. Model. Earth Syst. 12, e2019MS002010 (2020).
- 78. Bi, D. et al. Configuration and spin-up of ACCESS-CM2, the new generation Australian Community Climate and Earth System Simulator Coupled Model. *J. South. Hemisph. Earth Syst. Sci.* **70**, 225–251 (2020).
- Lovato, T. et al. CMIP6 simulations with the CMCC Earth System Model (CMCC-ESM2). J. Adv. Model. Earth Syst. 14, e2021MS002814 (2022).
- Döscher, R. et al. The EC-Earth3 Earth system model for the Coupled Model Intercomparison Project 6. Geosci. Model Dev. 15, 2973–3020 (2022).

Acknowledgements

We performed the SPEAR_LO and SPEAR_MED model experiments on the Gaea supercomputer at NOAA. We thank Drs. Isaac Held, Robert Hallberg, Mitch Bushuk, Nat Johnson, Hiroyuki Murakami, Pu Lin and Nadir Jeevanjee for providing constructive comments on our original research. The present research is supported by Princeton University/NOAA GFDL Visiting Research Scientists Program and base support of GFDL from NOAA Office of Oceanic and Atmospheric Research (OAR), JAMSTEC Overseas Research Visit Program, JSPS KAKENHI Grant Number JP22K03727.

Author contributions

Y.M. analyzed the data and model simulations and wrote the manuscript. W.C. conducted the model experiments. L.Z., W.C., M.N., S.B., and S.M. designed the research and contributed to the manuscript.

Competing interests

The authors declare no competing interests.

Additional information

Supplementary information The online version contains supplementary material available at https://doi.org/10.1038/s41467-024-54485-7.

Correspondence and requests for materials should be addressed to Yushi Morioka.

Peer review information *Nature Communications* thanks Charles Pelletier and the other, anonymous, reviewer(s) for their contribution to the peer review of this work. A peer review file is available.

Reprints and permissions information is available at http://www.nature.com/reprints

Publisher's note Springer Nature remains neutral with regard to jurisdictional claims in published maps and institutional affiliations.

Open Access This article is licensed under a Creative Commons Attribution-NonCommercial-NoDerivatives 4.0 International License, which permits any non-commercial use, sharing, distribution and reproduction in any medium or format, as long as you give appropriate credit to the original author(s) and the source, provide a link to the Creative Commons licence, and indicate if you modified the licensed material. You do not have permission under this licence to share adapted material derived from this article or parts of it. The images or other third party material in this article are included in the article's Creative Commons licence, unless indicated otherwise in a credit line to the material. If material is not included in the article's Creative Commons licence and your intended use is not permitted by statutory regulation or exceeds the permitted use, you will need to obtain permission directly from the copyright holder. To view a copy of this licence, visit http://creativecommons.org/licenses/by-nc-nd/4.0/.

© The Author(s) 2024